

# Nuclear quadrupole resonances in compact vapor cells: the crossover between the NMR and the nuclear quadrupole resonance interaction regimes

E.A. Donley, J.L. Long, T.C. Liebisch, E.R. Hodby, T.A. Fisher, and J. Kitching

*NIST Time and Frequency Division  
325 Broadway, Boulder, CO 80305*

(Dated: June 27, 2018)

We present an experimental study that maps the transformation of nuclear quadrupole resonances from the pure nuclear quadrupole regime to the quadrupole-perturbed Zeeman regime. The transformation presents an interesting quantum-mechanical problem, since the quantization axis changes from being aligned along the axis of the electric-field gradient tensor to being aligned along the magnetic field. The large nuclear quadrupole shifts present in our system enable us to study this regime with relatively high resolution. We achieve large nuclear quadrupole shifts for  $I = 3/2$   $^{131}\text{Xe}$  by using a cube-shaped  $1\text{ mm}^3$  vapor cell with walls of different materials. The enhancement of the NQR shift from the cell wall materials is a new observation that opens up an additional adjustable parameter to tune and enhance the nuclear quadrupole interactions in vapor cells. As a confirmation that the interesting and complex spectra that we observe are indeed expected, we compare our data to numerical calculations and find excellent agreement.

PACS numbers: 32.60.+i, 33.25.+k, 76.60.Gv

## I. INTRODUCTION

Any atom that has a nuclear spin  $I \geq 1$  has a nuclear electric quadrupole moment, whose interactions with electric field gradients can cause shifts of the nuclear magnetic energy levels. There is a large body of literature on the interactions of nuclear quadrupole moments with electric field gradients. As far back as the 1950s, studies were performed in crystals both in the regime where the nuclear quadrupole interaction caused weak perturbations to the nuclear magnetic resonance (NMR) spectra [1], as well as in the pure nuclear quadrupole resonance (NQR) regime, where little or no Zeeman interaction was present [2]. Solutions for the transition energies between nuclear spin sublevels were found for both regimes by use of perturbation theory (for a review, see [3]) by aligning the quantization axis along the principal axis of the electric field gradient tensor in the NQR regime and along the axis of the magnetic field in the NMR regime. As with these first experiments, most NQR studies have either been distinctly in either the NQR or the NMR regimes. To our knowledge, prior to our work reported here, the transformation of the NQR spectra from the NQR to the NMR regimes had not been observed experimentally.

Cohen-Tannoudji first suggested that in addition to arising from electric field gradients from ionic bonds in a crystal, quadrupolar coupling could occur between nuclei and electrical field gradients present at the nucleus during wall collisions for atoms in vapor cells [4]. Since then, nuclear quadrupole resonances in vapor cells have been studied for many systems including  $I = 3/2$   $^{201}\text{Hg}$  [5, 6, 7, 8, 9],  $I = 9/2$   $^{83}\text{Kr}$  [10],  $I = 3/2$   $^{131}\text{Xe}$  [11, 12, 13, 14, 15, 16], and  $I = 3/2$   $^{21}\text{Ne}$  [17]. Much of this work has been of basic interest from a fundamental physics standpoint [5, 6, 7, 10, 11, 12, 13, 14, 15, 16] and for tests of fundamental symmetries [8, 9, 17, 18]. There have also been proposals for using these systems for the practical application of rotation sensing [19, 20]. Changes to the NQR shifts in the crossover regime could lead to systematic errors in precision measurements and offsets in rotation

sensors.

For much of the NQR work that has been performed in vapor cells, the NQR lines were not clearly resolved and the NQR splitting caused a slow beating or a nonexponential decay of the nuclear polarization [5, 6, 7, 10, 11]. The beat frequencies depended on the orientation of the cell symmetry axis in the magnetic field, and went to zero at the magic angle of  $54.7^\circ$  [5], which indicated that the axis of symmetry of the electric field gradient was aligned along the cell symmetry axis.

In a series of papers from Happer's group at Princeton [12, 13, 14], Wu et al. saw much stronger interactions such that the NQR lines could be clearly resolved by using highly asymmetric cells. They performed a detailed perturbation-theory solution for the NQR shift in the NMR regime, accounting for pressure-dependent diffusion and cell shape, and formulated the results to give a microscopic description of the interaction [13]. Ignoring complications from diffusion, they expressed the NQR shifts for the  $|-3/2\rangle\langle -1/2|$  and  $|1/2\rangle\langle 3/2|$  coherences as

$$\Delta\Omega = \pm \frac{vS}{2V} \frac{1}{2I-1} \int_S \frac{dS'}{S} \langle \theta \rangle \left[ \frac{3}{2} \cos^2 \psi - \frac{1}{2} \right], \quad (1)$$

which is an integration of the nuclear quadrupole interaction over the cell walls. Here  $v$  is the atom velocity,  $\langle \theta \rangle$  is the mean twist angle per wall adhesion,  $S$  is the cell surface area,  $V$  is the cell volume,  $I$  is the nuclear spin, and  $\psi$  is the angle between the local surface normal (directed out of the cell) and the magnetic field. Here we put  $\langle \theta \rangle$  within the integral to allow for the possibility that the cell walls are of different materials. Integrating Eq. 1 for a cylindrical cell gives  $\Delta\Omega = \pm \Delta\Omega_0 P_2(\cos \varphi)$ , where  $\varphi$  is the angle between the cell symmetry axis and the direction of the magnetic field and  $P_2(x) = \frac{1}{2}(3x^2 - 1)$ .  $\Delta\Omega_0 = vA \langle \theta \rangle S/4V$  is proportional to the atom velocity, the surface to volume ratio of the cell, and an asymmetry parameter,  $A$ , which goes to zero when the cell height and diameter are equal. Wu et al. verified their theory with detailed experiments and determined

$(\theta) = 38(4) \times 10^{-6}$  rad for pyrex [14]. Experiments later performed by Butscher et al. [15] revealed similar behavior.

All of the experiments described so far were performed at magnetic fields high enough that the nuclear quadrupole interaction was well described as a perturbation to the magnetic Larmor resonances. Appelt et al. performed studies on  $^{131}\text{Xe}$  in the limit of zero applied magnetic field and measured deviations from Berry's adiabatic phase under rotation [16]. They solved the  $I = 3/2$  Hamiltonian by including terms for the NQR interaction and spatial rotations and showed that mixing of the nuclear spin sublevels through rotation makes all six transitions between nuclear sublevels allowed ( $\Delta m = 1, 2,$  and  $3$ ).

All of this work was either distinctly in the NMR [10, 11, 12, 13, 14, 15] or the NQR [16] regime. Here we bridged the two regimes by continuously tracing the transformation from the pure NQR regime to the quadrupole-perturbed Zeeman regime. We achieved a large NQR splitting not by using geometrically asymmetric cells as Wu et al. [12] did, but by using a  $1 \text{ mm}^3$  cubic cell with walls of different materials. A cubic charge distribution would not ordinarily cause an NQR splitting [7], but the microscopic surface interactions with the different wall materials lower the symmetry of the system. The small cell size enhances the NQR splitting because the shifts are proportional to the surface to volume ratio. The enhancement of the NQR shift from the cell wall materials is a new observation that gives one an additional adjustable parameter to tune the electric field gradient and the NQR interaction in vapor cells. As a confirmation that the complex spectra that we observe are expected, we compare the transformation of the resonance lines to theoretical models and find excellent agreement.

## II. EXPERIMENT

### A. Techniques and Apparatus

Fig. 1A is a schematic drawing of our apparatus. The microfabricated sample cell of volume  $1 \text{ mm}^3$  was etched in silicon and sealed with pyrex [21]. The cell contains  $^{87}\text{Rb}$ , buffer gases of  $\text{N}_2$  and  $\text{Ne}$  at 10 and 600 torr, respectively, and 10 torr of  $\text{Xe}$  gas at natural abundance.  $\text{Xe}$  has two active NMR isotopes: spin-1/2  $^{129}\text{Xe}$  (26.4% abundance) and spin-3/2  $^{131}\text{Xe}$  (21.2% abundance). The cell is cubic and has four silicon walls and two pyrex windows. The cell is heated to  $145^\circ\text{C}$  and mounted at the center of a set of three orthogonal magnetic coils. The coils are surrounded by a four-layer magnetic shield (one layer shown in Fig. 1A). A circularly polarized laser beam optically pumps and probes the  $\text{Rb}$  atoms through the pyrex cell windows along the  $\hat{z}$ -axis. The  $\text{Rb}$  polarizes the  $\text{Xe}$  atoms through spin-exchange optical pumping [22]. The  $\text{Rb}$  also functions as a magnetometer and is used to sense the magnetic fields generated by the  $\text{Xe}$  atoms [23, 24].

We use a field switch technique to initiate precession of the  $\text{Xe}$  atoms. During the pump phase, the  $\text{Xe}$  polarization builds and reaches steady state. At the start of the probe phase, a DC magnetic field,  $B_0$ , is turned on in the  $\hat{y}$ - $\hat{z}$  plane and the  $\text{Xe}$

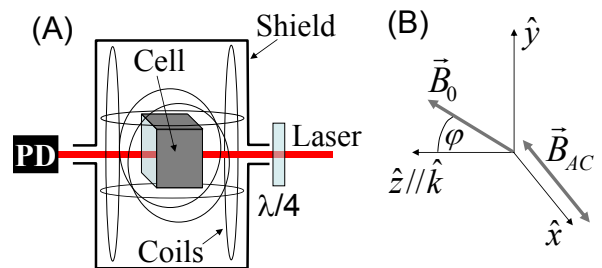


FIG. 1: (A). The apparatus. The  $1 \text{ mm}^3$  cell is roughly centered on an orthogonal three-axis set of magnetic coils. A laser beam of maximum power 3 mW enters the cell. The transmitted power is detected by a photodiode. (B). The coordinate system: the  $\hat{z}$ -axis coincides with the light propagation direction,  $\hat{k}$ . The magnetic field direction is in the  $\hat{y}$ - $\hat{z}$  plane rotated by an angle  $\varphi$  from the  $\hat{z}$ -axis.

atoms start to precess. The angle of  $\vec{B}_0$  with respect to the  $\hat{z}$ -axis (the cell symmetry axis),  $\varphi$ , is varied, depending on the experiment. An AC magnetic field,  $\vec{B}_{AC}$ , of rms amplitude  $\sim 1 \mu\text{T}$  and frequency  $\sim 2 \text{ kHz}$  drives the  $\text{Rb}$  atoms and is applied along the  $\hat{x}$ -axis. This AC drive also references a lock-in amplifier that measures the modulation of the transmitted power at the  $\text{Rb}$  drive frequency. The applied field geometry is shown in Fig. 1B. We are also able to observe signals in many other field configurations, but we have found this configuration to give the best signal-to-noise ratio. Our geometry for pumping and probing is very similar to the technique used by Volk et al. [25].

After a field switch, a free induction decay (FID) signal is observed at the output of the lock-in amplifier. Fig. 2 shows an FID signal and its Fourier transform. In most cases, we used an acquisition time of 32.8 s on our spectrum analyzer, which gave a frequency resolution of 30.5 mHz. Since the acquisition time was much longer than our typical  $T_2$  time of  $\sim 5 \text{ s}$ , we compromised on signal-to-noise ratio to achieve higher frequency resolution.

One factor that complicates our estimating the field magnitude and angle is the relatively large field generated by the  $\text{Rb}$  atoms as sensed by the  $\text{Xe}$  atoms [26], the magnitude of which is  $B_{Rb} = \mu_B \frac{8\pi\kappa}{3} \frac{\mu_0}{4\pi} n_{Rb} P$ .  $\mu_B$  is the Bohr magneton,  $\kappa = 730$  is the hyperfine contact enhancement factor [27],  $\mu_0$  is the magnetic constant,  $n_{Rb}$  is the  $\text{Rb}$  density, and  $P$  is the  $\text{Rb}$  polarization. At our laser intensity of  $300 \text{ mW/cm}^2$  and temperature of  $145^\circ\text{C}$ , we measure  $B_{Rb} = 200 \text{ nT}$ , which corresponds to  $P = 30\%$ .

To simplify controlling the total field in the presence of this large offset field, for most of our measurements we divide our applied field into two components such that our total field is  $\vec{B}_{tot} = \vec{B}_0 + \vec{B}_{Rb} + \vec{B}_{comp}$ . We set the compensation field,  $\vec{B}_{comp}$ , equal to  $-\vec{B}_{Rb}$ , such that we can determine our total field as sensed by  $\text{Xe}$  from the variable component  $\vec{B}_0$  alone. Offsetting  $\vec{B}_{Rb}$  is made easier by having a high pumping rate so that  $\vec{B}_{Rb} \parallel \hat{k}$  is independent of the angle of  $\vec{B}_0$ . Then  $\vec{B}_{Rb}$  can be nulled out with a constant field parallel to the direction of light propagation. This approach simplifies controlling

both  $\varphi$  and the total field as the angle or magnitude of  $\vec{B}_0$  is varied.

### B. Measurements

We concentrate our measurements on two things: first, the  $^{131}\text{Xe}$  NQR shift  $\Delta\Omega$  versus angle  $\varphi$ , and second, the transformation of the energy shifts as  $B_0$  is swept from zero through the NQR-dominated regime and into the NMR-dominated regime. To measure  $\Delta\Omega$  (Eq. 1) versus  $\varphi$ ,  $B_0$  was kept near  $0.8\ \mu\text{T}$ . At high enough field, the NQR splitting depends on the field angle but not on the field magnitude. For this measurement, we did not apply a compensation field as described above, but rather included  $\vec{B}_{Rb}$  in our calculation of  $\varphi$ . The data were consistent with  $\vec{B}_{Rb} \parallel \hat{k}$ . We measured the  $^{129}\text{Xe}$  and  $^{131}\text{Xe}$  spectra versus angle at two different laser powers:  $0.6\ \text{mW}$  and  $3\ \text{mW}$  ( $60$  and  $300\ \text{mW}/\text{cm}^2$ ). We determined frequency differences between the outer two  $^{131}\text{Xe}$  resonances using curve fitting and took  $\Delta\Omega$  to be half of the difference. The inset in Fig. 2B is a plot of  $\Delta\Omega$  versus  $\cos\varphi$  for two different laser powers. Only field angle values where the triplet is resolved for curve fitting are included. The parabolic fit of the data agrees well with  $\Delta\Omega = 0$  at the magic angle of  $\varphi = 54.7^\circ$  ( $\cos\varphi = 0.578$ ).

To make quantitative estimates of the mean rotation angle per wall collision, we apply Eq. 1 to our cubic cell. Assuming  $\langle\theta\rangle$  for pyrex can be expressed in terms of  $\langle\theta\rangle$  for silicon as  $\langle\theta_p\rangle = \langle\theta_s\rangle + \delta$  one finds  $\Delta\Omega = \Delta\Omega_0 P_2(\cos\varphi)$ , where  $\Delta\Omega_0$  reduces to  $v\delta/L$ .  $L$  is the length of a side of the cube, and  $v$  is the mean thermal velocity. Fitting this expression to the data in the inset of Fig. 2B, we find  $\Delta\Omega_0 = 2\pi \times 0.39\ \text{Hz}$ . With  $L = 1\ \text{mm}$ , and  $v = 281\ \text{m/s}$ , we find  $\delta = 8.7\ \mu\text{rad}$ . Using Wu et al.'s measurement of  $\langle\theta_p\rangle = 38\ \mu\text{rad}$  for pyrex [14], we find  $\langle\theta_s\rangle = 29\ \mu\text{rad}$  for silicon.

To measure the spectra versus field magnitude for a fixed field angle, we carefully offset  $\vec{B}_{Rb}$  by applying a compensation field along  $\hat{k}$ . We collected multiple spectra versus field magnitude at several field angles. Data are presented in Fig. 3 for  $\varphi = 22^\circ$  and  $39^\circ$ . The plots are three-dimensional – the vertical axis is the measured frequency, the horizontal axis is the applied magnetic field (not counting  $B_{comp}$ ), and the symbol size is proportional to the signal amplitude. Each vertical line represents an individual frequency spectrum collected at a fixed magnetic field. The black lines show the transition frequencies for  $^{129}\text{Xe}$  versus magnetic field. Since  $^{129}\text{Xe}$  has no nuclear electric quadrupole moment, the transition energy is linear in applied field. The gray lines represent the energy differences between the four nuclear sublevels of  $^{131}\text{Xe}$  found numerically, as discussed below.

### III. CALCULATIONS

In the limit that the NQR shift is either much smaller or much larger than the Larmor frequency, perturbation theory solutions accurately predict the transition frequencies [2, 10].

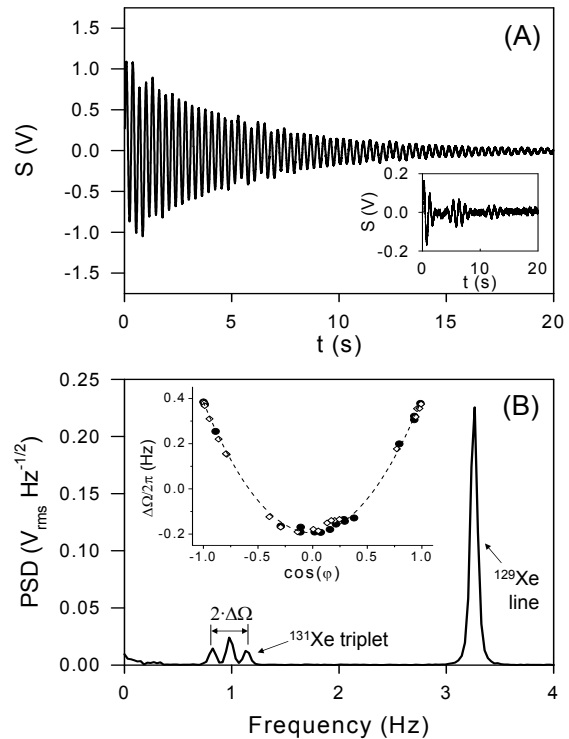


FIG. 2: Examples of experimental data. (A). A free-induction decay. The signal is proportional to the amplitude of the modulation of the photodiode signal caused by the Rb precession and is presented in volts. The magnetic field during the probe phase was  $275\ \text{nT}$ , and  $\varphi$  was  $\sim 70^\circ$ . Beating from the  $^{131}\text{Xe}$  triplet is seen in inset, which shows the residuals from a fit of a damped sine wave to the data. (B). The Fourier transform of the data in (A). Here the signal is presented as a power spectral density in the units of root-mean-squared volts in a  $1\ \text{Hz}$  bandwidth. The inset is a plot of the NQR splitting versus  $\cos\varphi$ . The solid symbols are data collected at  $300\ \text{mW}/\text{cm}^2$ , and the open symbols are data collected at  $60\ \text{mW}/\text{cm}^2$ . For the low (high) power data, the Rb field was  $0.12\ \mu\text{T}$  ( $0.19\ \mu\text{T}$ ). For comparison, the applied field was  $\sim 0.8\ \mu\text{T}$ . There is more distortion in the parabolic shape of the curve for the low power data – particularly when the applied field was orthogonal to the light propagation direction where the approximation that  $B_{Rb} \parallel \hat{k}$  would not hold as well. The dashed line is a fit to the high-power data, which gives a value of  $\Delta\Omega_0/2\pi = 0.39(1)\ \text{Hz}$ . Our value for  $\Delta\Omega_0$  is  $\sim 43\%$  larger than the largest value reported by Wu et al. [14].

When the NMR and NQR interactions are of comparable size, a more involved solution is required. It is possible to solve the system analytically by diagonalizing the full Hamiltonian to find the transition energies as well as the transition amplitudes [28], but it is involved – particularly given the dynamics and the angular sensitivity of the Rb magnetometer. Finding the full analytical solution is made dramatically more accessible by taking as a starting point a general solution that has already been developed and is available online [29]. A full calculation yielding predictions for the line amplitudes that will give more insight into the physics is underway and will be reported elsewhere. For this work, we compare our data to numerical

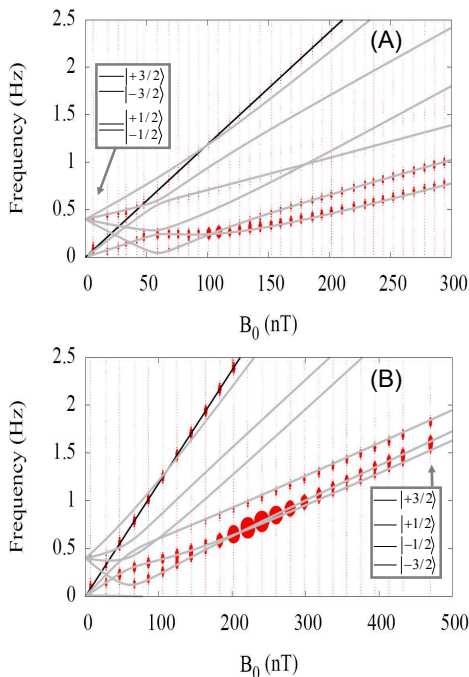


FIG. 3: Spectra versus applied field for  $\varphi = 22^\circ$ (A) and  $\varphi = 39^\circ$ (B). The grey lines represent the six frequency differences between the four nuclear sublevels computed numerically (see text). The black lines mark the  $^{129}\text{Xe}$  transition versus field. Each vertical line represents a different frequency spectrum acquired at the specific magnetic field that it intersects on the horizontal axis. The symbol size is proportional to the signal amplitude, and the same amplitude scale was used for both angles of  $\varphi$ . The laser intensity was  $300 \text{ mW/cm}^2$  and  $B_{Rb}$  was  $0.19 \mu\text{T}$ . The inset in (A) shows the  $^{131}\text{Xe}$  nuclear energy levels in the low-field NQR regime. Since the energies of the nuclear sublevels go as  $m^2$  at zero magnetic field [1], the  $|+3/2\rangle$  and  $|-3/2\rangle$  states are degenerate at zero field, as are the  $|+1/2\rangle$  and  $|-1/2\rangle$  states. The inset in (B) shows the nuclear energy levels in the high-field NMR regime.

calculations using a Liouvillian approach described in detail by Bain [30]. The method is relatively straightforward to use for calculating the transition frequencies for an arbitrary spin nucleus in an arbitrary magnetic field and electric field gradient, but it does not predict the transition amplitudes and it is also not very transparent. The details of the calculation are outside of the scope of this article, and we refer the interested reader to the original work [30], which gives the recipe for the calculations.

Three parameters enter the calculation: the angle  $\varphi$ ,  $\Delta\Omega_0$ , and an asymmetry parameter,  $\eta$ , which is zero in the case of a cylindrically symmetric electric field gradient. We set  $\eta = 0$  for our simulations and for  $\Delta\Omega_0$  we use our measurement from the inset of Fig. 2B. We used our estimates of  $\varphi$  from our coil calibrations and cell orientation assuming the symmetry axis of the electric field gradient to be along the cell symmetry axis. We conservatively estimate an upper limit of  $5^\circ$  for angular misalignment of the cell axis from the magnetic field axis.

The gray lines presented in Fig. 3 are the six transition fre-

quencies between the four nuclear states. At high magnetic fields in the NMR regime, there are three lines with equal slope, corresponding to  $\Delta m = 1$  transitions ( $|-3/2\rangle\langle-1/2|$ ,  $|-1/2\rangle\langle1/2|$ , and  $|1/2\rangle\langle3/2|$ ), two lines with double the slope for  $\Delta m = 2$  transitions ( $|-3/2\rangle\langle1/2|$  and  $|-1/2\rangle\langle3/2|$ ), and one line for the  $\Delta m = 3$  transition ( $|-3/2\rangle\langle3/2|$ ). Note that these transition frequencies are plotted with no insight into the transition amplitudes, and in fact, only the  $\Delta m = 1$  transitions are allowed at higher fields. At very low magnetic field,  $\Delta m = 1, 2,$  and  $3$  transitions are also seen, but they do not correspond to the same  $\Delta m = 1, 2,$  and  $3$  transitions seen at higher field because the quantization axis rotates as a function of magnetic field thus transforming the states.

The observed  $^{131}\text{Xe}$  lines agree well with the predicted frequencies even as the magnetic field goes to zero. At low field, the transitions are unresolved, and in most cases it is difficult to assign features to  $\Delta m = 2$  or  $\Delta m = 3$  transitions. Perhaps the best resolved spectrum at low field, where we would expect strong mixing of the lines, was collected for  $28 \text{ nT}$  and  $\varphi = 39^\circ$ , which corresponds to the second spectrum from the left in Fig. 3B. This spectrum is shown in Fig. 4. The predicted transition frequencies are marked. One of the  $\Delta m = 2$  transitions is clearly visible and is one-tenth as strong as the  $\Delta m = 1$  transitions. The other  $\Delta m = 2$  transition and the  $\Delta m = 3$  transition are not visible. We cannot put limits on the strength of the  $\Delta m = 3$  transition, since the frequency where it would appear is obscured by the wings of other, much stronger transitions.

#### IV. DISCUSSION AND OUTLOOK

One point requiring further investigation relates to the amplitudes of the  $^{131}\text{Xe}$  lines. Whereas the  $^{129}\text{Xe}$  line amplitudes vary by about 10% as  $B_0$  is varied, the  $^{131}\text{Xe}$  line amplitudes vary by much more – sometimes jumping up by a

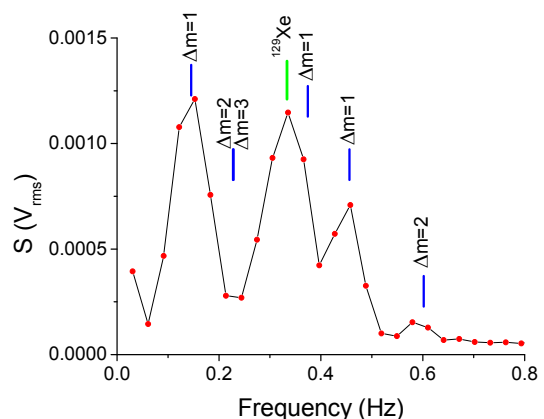


FIG. 4: A single spectrum collected with  $28 \text{ nT}$  and  $\varphi = 39^\circ$ , which corresponds to the second spectrum from the left in Fig. 3. The predicted transition frequencies are also shown for reference. The signal has the units of root-mean-squared amplitude for a  $32.768 \text{ s}$  averaging time. Given that the  $T_2$  time is about  $5 \text{ seconds}$ , we compromised on signal amplitude to achieve improved frequency resolution.

factor of 2 to 3 when the lines cross, and sometimes fading away and disappearing at a different field. The variations in line amplitudes for  $^{131}\text{Xe}$  will be the subject of further study in conjunction with performing a full analytical solution.

Our NQR shifts are large enough that we are able to measure the decay rates for the individual lines. Like the line amplitudes, the decay rates for the  $^{131}\text{Xe}$  lines vary widely – especially at the line crossings. The ratio of the decay rates for the  $|-3/2\rangle\langle-1/2|$  and  $|1/2\rangle\langle3/2|$  coherences relative to the  $|-1/2\rangle\langle1/2|$  coherence does not agree with the 3:2 result predicted by Wu et al. for the NMR regime [13]. The variation in the decay rates will also be an area of further study.

## ACKNOWLEDGMENTS

We thank Michael Romalis for initially suggesting that we study this very interesting regime, Simon Rochester and Dmitry Budker for assistance with and insight into the theoretical calculations, and Will Happer, Hugh Robinson, Svenja Knappe, Susan Schima, and Leo Hollberg for technical assistance and discussions. This work was funded by DARPA and is a contribution of NIST, an agency of the US government, and is not subject to copyright.

- 
- [1] R. V Pound, Phys. Rev. **79**, 685 (1950)
  - [2] M. Bloom, E. L. Hahn, B. Herzog, Phys. Rev. **97**, 1699 (1955)
  - [3] A. Abragam, *The Principles of Nuclear Magnetism*, (Oxford University Press, 1961)
  - [4] C. Cohen-Tannoudji, J. Phys. (Paris) **24**, 653 (1963)
  - [5] J. H. Simpson, Bull. Am. Phys. Soc. **23**, 394 (1978)
  - [6] P. A. Heimann, Phys. Rev. A **23**, 1204 (1981)
  - [7] P. A. Heimann, I. A. Greenwood, J. H. Simpson, Phys. Rev. A **23**, 1209 (1981)
  - [8] S. K. Lamoreaux, J. P. Jacobs, B. R. Heckel, F. J. Raab, E. N. Fortson, Phys. Rev. Lett. **57**, 3125 (1986)
  - [9] S. K. Lamoreaux, J. P. Jacobs, B. R. Heckel, F. J. Raab, E. N. Fortson, Phys. Rev. A **39**, 1082 (1989)
  - [10] C. H. Volk, J. G. Mark, B. C. Grover, Phys. Rev. A **20**, 2381 (1979)
  - [11] T. M. Kwon, J. G. Mark, C. H. Volk, Phys. Rev. A **24**, 1894 (1981)
  - [12] Z. Wu, W. Happer, J. M. Daniels, Phys. Rev. Lett. **59**, 1480 (1987)
  - [13] Z. Wu, S. Schaefer, G. D. Cates, W. Happer, Phys. Rev. A **37**, 1161 (1988)
  - [14] Z. Wu, W. Happer, M. Kitano, J. Daniels, Phys. Rev. A **42**, 2774 (1990)
  - [15] R. Butscher, G. Wäckerle, M. Mehring, J. Chem. Phys. **100**, 6923 (1994)
  - [16] S. Appelt, G. Wäckerle, M. Mehring, Phys. Rev. Lett. **72**, 3921 (1994)
  - [17] T. E. Chupp, R. J. Hoare, Phys. Rev. Lett. **64**, 2261 (1990)
  - [18] P. K. Majumder, B. J. Venema, S. K. Lamoreaux, B. R. Heckel, E. N. Fortson, Phys. Rev. Lett. **65**, 2931 (1990)
  - [19] J. H. Simpson, *Astronautics & Aeronautics* **2**, 42 (1964)
  - [20] B. C. Grover, E. Kanegsberg, J. G. Mark, R. L. Meyer, U.S. Patent No. **4,157,495**, (1979)
  - [21] S. Knappe, V. Gerginov, P. D. Schwindt, V. Shah, H. G. Robinson, L. Hollberg, and J. Kitching, Opt. Lett. **30**, 2351 (2005)
  - [22] T. G. Walker, W. Happer, Rev. Mod. Phys. **69**, 629 (1997)
  - [23] B. C. Grover, Phys. Rev. Lett. **40**, 391 (1978)
  - [24] G. M. Keiser, H. G. Robinson, C. E. Johnson, Phys. Rev. A **16**, 822 (1977)
  - [25] C. H. Volk, T. M. Kwon, J. G. Mark, Phys. Rev. A **21**, 1549 (1980)
  - [26] S. R. Schaefer, G. D. Cates, T. R. Chien, D. Gonatas, W. Happer, T. G. Walker, Phys. Rev. A **39**, 5613 (1989)
  - [27] T. G. Walker, Phys. Rev. A **40**, 4959 (1989)
  - [28] S. M. Rochester, D. Budker, Private Communication (2008)
  - [29] <http://budker.berkeley.edu/ADM/index.html>
  - [30] A. D. Bain, Mol. Phys. **101**, 3163 (2003)